Time-Lapse Imaging of Human Heart Motion With Switched Array UWB Radar

Sverre Brovoll, Tor Berger, Yoann Paichard, *Member, IEEE*, Øyvind Aardal, Tor Sverre Lande, *Fellow, IEEE*, and Svein-Erik Hamran

Abstract—Radar systems for detection of human heartbeats have mostly been single-channel systems with limited spatial resolution. In this paper, a radar system for ultra-wideband (UWB) imaging of the human heart is presented. To make the radar waves penetrate the human tissue the antenna is placed very close to the body. The antenna is an array with eight elements, and an antenna switch system connects the radar to the individual elements in sequence to form an image. Successive images are used to build up time-lapse movies of the beating heart. Measurements on a human test subject are presented and the heart motion is estimated at different locations inside the body. The movies show rhythmic motion consistent with the beating heart, and the location and shape of the reflections correspond well with the expected response form the heart wall. The spatial dependent heart motion is compared to ECG recordings, and it is confirmed that heartbeat modulations are seen in the radar data. This work shows that radar imaging of the human heart may provide valuable information on the mechanical movement of the heart.

Index Terms—Antenna array, electromagnetic propagation in absorbing media, heart, medical radar, MIMO radar, radar imaging, ultra wideband radar.

I. Introduction

CARDIOVASCULAR DISEASES (CVD) are a major cause of deaths worldwide [1]. Radar technology has the potential to give valuable clinical information about the mechanical dynamics of the heart, and can be a valuable tool for diagnostics of CVD. By placing the radar antennas in contact with or very close to the human body, the strong reflection from the air-body surface is reduced and the radar is able to sense waves that penetrate the tissue and are reflected from the heart wall [2]. In this way the radar directly measures the mechanical movement of the heart, and can noninvasively provide information for heart diagnosis.

Microwave detection of vital signs including heart rate has been reported in the literature [3]–[5]. For the radar to be an interesting tool for diagnostics of CVD, additional information on the cardiovascular process is required. In [6] and [7] heartbeat signals were recorded with body-contact single channel continuous wave radars. Several details of the cardiac cycle were identified, including the opening and closing of the cardiac valve and ventricular ejection and filling. In [7] it was also shown that the heartbeat waveform was dependent on blood pressure and/or heart rate. These studies show that body-contact radar is sensitive to details regarding the cardiac cycles beyond detection of heart rate. If these details can be reliably quantized and measured, medical radar can be a viable sensor for diagnostics of CVD.

Similar measurements as in [6] were performed in [8]. Here radar recordings were conducted with the antenna positioned at different locations on the thorax. The results showed that the recorded waveforms differ significantly at different antenna locations. This indicates that the radar sensor detects different cardiac movements inside the body at different antenna positions. With imaging radar it is possible to simultaneously measure how different parts of the heart are moving. This can give valuable information on the physical state of the heart.

Biomedical microwave imaging has been widely reported in the literature, mainly for the application of breast cancer detection. The reported systems can be divided in two main categories, microwave tomography [9], [10], and radar-based systems [11]–[15]. The human thorax presents a very complex medium for electromagnetic (EM) wave propagation and it is not clear if radar imaging can give valuable results without using complicated microwave tomography systems as in [16]. If a radar imaging system is to be a relevant tool for heart monitoring and diagnostics of CVD, it must be relatively simple, easy to use and inexpensive compared to other high resolution medical imaging modalities like MRI.

In this paper the feasibility of radar imaging of the human heart is studied using a simplistic radar system based on a vector network analyzer (VNA), a switched array system and a delay and sum (DAS) based beamformer. This is the same approach used by the radar-based systems for breast-cancer detection that have been used in clinical trials on patients [11]–[13], although in [11] a mechanical scan system was used to synthesize the antenna array. The robustness and simplicity of the DAS beamformer makes it a good choice for this study.

The breast cancer systems have been studied with the use of breast phantoms. A phantom of the human thorax with beating heart and internal organs are complicated to construct with a re-
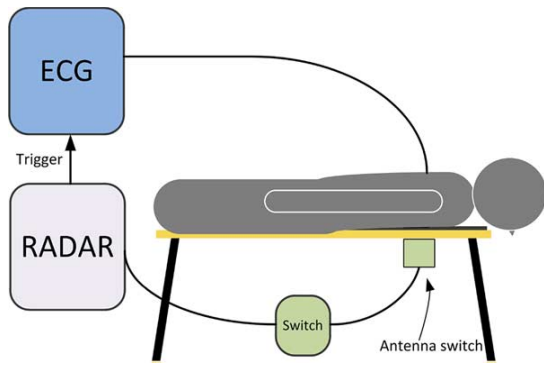
Fig. 1. The antenna array was laid on top of a radar absorbent mat on a wooden table, see Fig. 6. The test subject was lying face down on top of the table with the antenna center at the middle of the sternum.

alistic level of fidelity. In this feasibility study we therefore use measurements on a patient. The drawback is that it is difficult to give quantitative evaluation of the performance since the body interior is unknown. However, if promising results are achieved with this system, medical imaging of the heart using radar is an interesting topic for further studies. It is also an interesting field for the use of novel UWB radar circuits as described in [17] and [18].

The radar system is detailed in Section II, and the imaging algorithm is presented in Section III.C. Additional signal processing of the data is described in Section IV. Measurements on a male person were carried out with two different antenna configurations. The measurements are described in Section II.A and the results are presented in Section V and discussed in Section VI.

II. System Description

A. Measurement Description

Imaging of the heart was performed on a 35 year old male test subject. Figs. 1 and 6 shows the measurement setup. The antenna was visually aligned with the body, the center of the antenna at the sternum, and the extreme elements at the center of each pectoral muscle. Between each measurement the person had to leave the measurement table, therefore small deviations in the alignment between the antenna and the body are expected. The person was holding his breath, with the lungs inflated, during the measurements.

Imaging was carried out with two antenna configuration, described in detail in Section III.D. ECG recordings were done simultaneously, and by connecting a trigger signal directly to the ECG electrodes, the trigger sent when the radar started measuring was visible directly in the ECG data. This allows us to synchronize the ECG and radar recordings.

B. Switch System

The radar system is illustrated in Fig. 2. With a switch system we are able to use a Rohde & Schwarz ZVA110 VNA as radar front-end in our imaging system. The switch connects the different antenna elements to the transmit (Tx) and receive (Rx) ports of the VNA in sequence, giving the spatial sampling needed for image formation.

The switch system consists of two 1:8 switches, one for the Tx channel and one for the Rx channel. At each antenna element
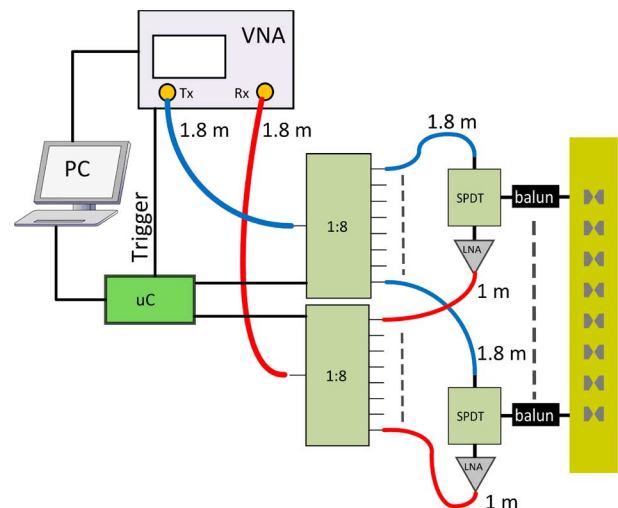

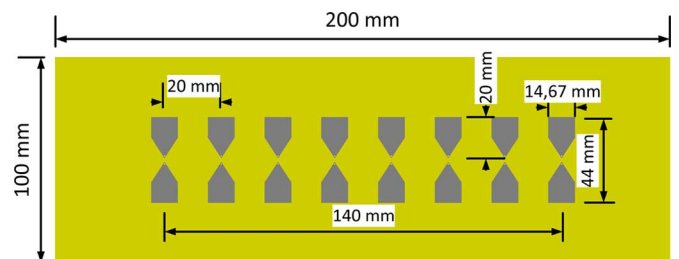Fig. 2. Block diagram of the radar system.

Fig. 3. A drawing of the antenna array. The array is manufactured on one PCB, and SMA connectors are soldered on at the back of each element. The elements are bow-tie dipoles and the dimensions of the elements are given at element number 8.

a single pole double throw (SPDT) switch is connected. The SPDT switch controls whether the element is connected to the Tx port or Rx port. In this manner every element in the antenna can be configured as an Rx element or a Tx element.

Evaluation boards from Hittite Microwave Corporation were used to build up the switch system. A low noise amplifier (LNA) with 12 dB gain is connected directly after the SPDT at the Rx channel. A balun consisting of a semi-rigid coaxial cable going through a tube of ferrites connects the switch to the antenna elements. The switches are controlled with a microcontroller; it reads the pulse trigger from the VNA and selects the Rx/Tx configuration between each pulse according to a switch pattern which is loaded from a PC.

C. Antenna

In [19] a uniform linear array where all the elements had equal spacing of 20 mm was used. In this work a nonuniform linear array with different element spacings is used. This gives a wider array and improved spatial sampling properties. The array is illustrated in Fig. 3, and the positions of the antenna elements are given in Table I.

A simple analysis of the array's spatial sampling properties is done by defining a virtual array with virtual element positions given by

$$x_{\mathrm{ve}}(n) = \frac{x_{tx}(n) + x_{rx}(n)}{2}, \quad n = 1, 2, \ldots, 56. \quad (1)$$

TABLE I
POSITION OF THE ANTENNA ELEMENTS

Element number:	1	2	3	4	5	6	7	8
x position [cm]:	0	5	8	10	12	14	17	22

Fig. 4. Position of unique virtual elements in cm along the positive x-axis starting at element number 1 in Fig. 3. The center of the black rectangles represents the position.

For element combination n, x_{ve} is the position of the virtual element, x_{tx} is the position of the transmitting element and x_{rx} is the position of the receiving element. Since there are eight elements in the array, and the same element cannot be used as both transmitter and receiver simultaneously, the maximum number of transmit/receive pairs is 56, hence the length of the vector of virtual elements. In the vector of virtual element positions there are 23 unique elements and their positions are illustrated in Fig. 4.

There are three different element spacings in the virtual array. The spacing between the two extreme elements at both ends is 1.5 cm and the spacing between the elements in the four densest groups is 0.5 cm. Between the other elements the spacing is 1 cm. As discussed later in Section III.A we use $\varepsilon_r = 22$ as an approximation for the relative permittivity of human tissue. In such a medium the wavelength is approximately 3 cm when the frequency is 2 GHz. The virtual array meets the spatial sampling criteria of maximum half a wavelength element spacing up to 2 GHz. From 2–3 GHz it is only the spacing between the two extreme elements at both ends that violate the sampling criteria. This array can be expected to behave well up to this frequency.

D. Radar

The VNA is configured as a step frequency radar [20]. The waveform is generated by transmitting N_p frequencies with a fixed frequency interval, Δf, over a given frequency band. After mixing the received and transmitted waveforms, the complex sampled signal is

$$S(f_n) = A(\tau)e^{-j2\pi f_n \tau}, \quad n = 1, 2, \ldots, N_p \tag{2}$$

where τ is the two way travel time for the received signal and A is an amplitude factor describing the reflectivity. By taking the inverse Fourier transform of (2) we get a range profile of the scene reflectivity

$$s(\tau) = \mathcal{F}^{-1}\{S(f_n)\} \tag{3}$$

were $s(r)$ is available through $r = \tau v_p$, and v_p is the velocity of propagation for the radar wave.

The instrumented range R_i is the maximum range to a target the radar can measure without spatial aliasing. The Nyquist sampling theorem states that it is the frequency sampling interval Δf that determines the instrumented range through

$$R_i = \frac{v_p}{2\Delta f} \tag{4}$$

where

$$\Delta f = \frac{B}{N_p - 1} \tag{5}$$

and B is the bandwidth of the transmitted waveform.

The velocity of propagation in a dielectric medium is given by

$$v_p \approx \frac{c}{\sqrt{\varepsilon_r}} \tag{6}$$

were c is the speed of light in vacuum and ε_r is the relative permittivity of the medium [21]. This relation holds for dielectric mediums, but body tissues are lossy materials and v_p also depends on the conductivity. As discussed later in Section III.A, we do not know the exact value for ε_r, and the uncertainties in our approximation of ε_r is higher than the effect of neglecting the conductivity in (6).

Using (6) together with (4) and (5) we can write the instrumented range as a function of the programmable VNA parameters B and N_p

$$R_i = \frac{c(N_p - 1)}{2B\sqrt{\varepsilon_r}}. \tag{7}$$

To image a dynamic object like the beating heart we want the VNA to have a high equivalent pulse repetition frequency (PRF). There are three parameters of the VNA that determine its PRF, which are B, N_p and the bandwidth of the IF filter in the VNA, B_{IF}. This value is programmable, and a smaller IF bandwidth gives lower thermal noise in the VNA receiver at the expense of a lower PRF due to a longer measurement time in the VNA.

In [19] the frequency range was 0.5–3 GHz, giving a bandwidth of 2.5 GHz. 151 frequencies were used and with an IF bandwidth of 1 MHz the PRF was approximately 328 Hz. In this work we would prefer a higher PRF, but at the same time decrease the IF bandwidth to get a better signal to noise ratio. To achieve this, the bandwidth and the number of frequencies have to be reduced.

E. Bandwidth

To analyze how much of the bandwidth that contributes to the formation of the radar images, data from [19] were used. The data was high-pass filtered to remove contribution from static reflectors, and then time-lapse images at 250 different sub bands were constructed. The time mean of the time-lapse images in a sub band were calculated to get one image of the mean power for each sub band. The sub bands were 250 MHz wide and centered around 250 different center frequencies from 625 MHz to 2875 MHz. The mean spatial power was calculated for every sub band and the results are plotted in Fig. 5. By reducing the frequency range to 0.75–2.27 GHz, we keep the images with mean power over the -10 dB line in Fig. 5. Although this implies a theoretical decrease of range resolution, the effective resolution is less affected since the removed frequencies contribute less to the image formation. This corresponds well to the findings in [22] where measurements on a breast cancer phantom showed
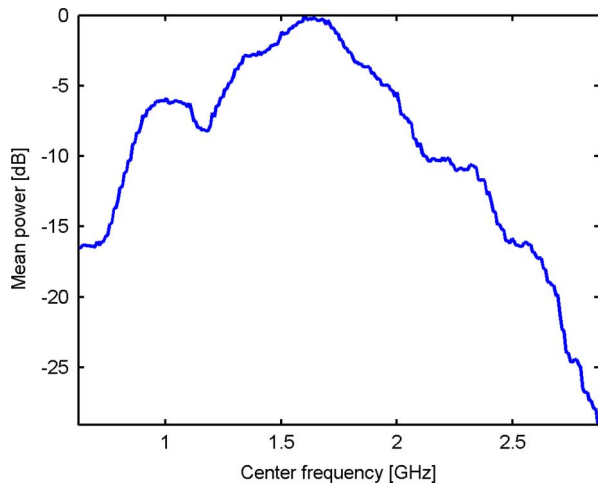
Fig. 5. Mean power in sub images created from a 250 MHz sub band around the center frequency. The power is calculated from the data used in [23].
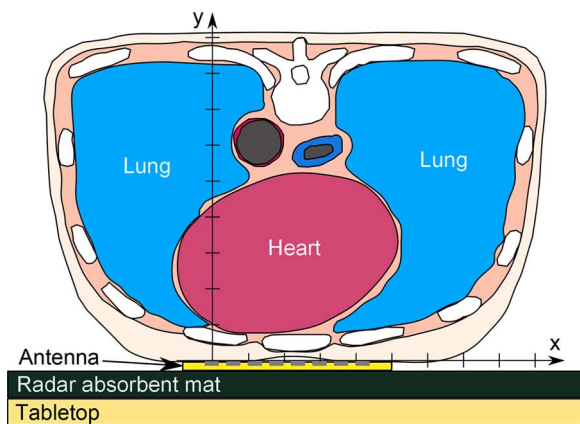

Fig. 6. A simple sketch of a cross-section of a general human thorax (redrawn from [27]) lying on top of a table. The antenna is seen below the thorax, and the drawn axes indicate the image axes used in the image processing. The dotted rectangle roughly indicates the size and position of the imaged area.

that the response from the low frequencies dominated the resulting image. The higher frequencies, 1–9 GHz in this case, contributed less to the detection of the tumor.

F. Number of Frequency Points

In [19] the length of the cables between the radar and the antenna was accounted for when calculating the instrumented range. Reflections from switch system and connectors will be suppressed by calibration (see Section IV.A) and the image processing. We therefore omit the cable length from the calculation of instrumented range. In this work we use 21 frequency points. By using $\varepsilon_r = 22$ and a bandwidth of 1.52 GHz, as described in the previous section, we get by using (4) an instrumented range of 42 cm. Due to the high attenuation in human tissue, reflectors deeper than the instrumented range are assumed attenuated enough to be invisible if they are folded back into the image.

G. Radar Settings

Due to the high attenuation of radar waves in the human tissue the reflected signals are very weak. Therefore we want as low IF-bandwidth as possible to get a low noise level in the

Parameter	Symbol	value
Frequency range	f	0.75 - 2.27 GHz
Bandwidth	B	1.52 GHz
Number of frequency points	N_p	21
Power	P	20 dBm
IF-bandwidth	B_{IF}	50 kHz
Pulse repetition frequency	PRF	820 Hz
Frame rate switch pattern 56	FR_{56}	14.6 Hz
Frame rate switch pattern 23	FR_{23}	35.6 Hz

TABLE III
A SIMPLE LAYERED BODY MODEL

Layer	Tissue	Relative Permittivity
1 (2 mm)	Skin	39.6
2 (13 mm)	Fat	5.4
3 (10 mm)	Muscle	54.0
4 (25 mm)	Bone	2.60

VNA. We found $B_{\text{IF}} = 50$ kHz to be a good tradeoff between noise level and PRF. The radar settings used are summarized in Table II. Note that the last two entries are explained in Section III.D, but listed here for completeness.

III. IMAGING

A. Electromagnetic Properties of Human Tissues

Table III describes a simple layered model of the tissues between the chest surface and the heart. This is the same model used in [23], and similar to the model used in [24]. The layers are numbered successively from the layer at the chest surface to the layer closest to the heart with the thickness given in parenthesis. A database of the electromagnetic properties of human tissues, based on the work in [25] is available online at [26]. In Table III we have used the data from [26] to calculate the mean value for the relative permittivity (ε_r) over the frequency range 0.75–2.27 GHz.

The relation between permittivity and velocity of propagation is given in (6), and from the values in Table III it is evident that the human body is a complicated inhomogeneous medium for EM wave propagation. For correct imaging with radar we ideally need a complete 3D-model of the distribution of the different tissues in the region we want to image. Both the spatial distribution of the tissues and their electromagnetic parameters are likely to vary from individual to individual, and a usable generic model will be very difficult, if possible, to construct. Such an approach is beyond the scope of this work. We therefore assume that the tissues are homogeneous with constant permittivity.

Using data from Table III, the mean permittivity, weighted with the thickness of the tissue layers, is calculated to be $\varepsilon_r \approx 22$. In such a medium the wavelength at the maximum frequency ($f_{\max} = 2.27$ GHz) is $\lambda = 2.85$ cm. The heart is only a couple of wavelengths away from the antenna, and the individual tissue layers are only a fraction of a wavelength thick. With the resolution of the radar system, and the short travel length for the radar
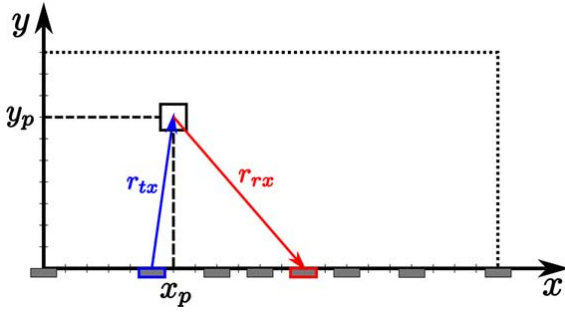
Fig. 7. Illustration of the geometry used in the back projection algorithm.

signals, good results can be achieved even with this very simplified model.

B. Imaging Geometry

The antenna array is described in Section II.C, and a sketch of the antenna and the image coordinate axis with respect to the human body is given in Fig. 6. The antenna is oriented along the x-axis, and the y-axis pointing into the human body. The body is oriented with the head in the negative z direction. The origin of the coordinate system is placed at the location of the first element of the antenna array. This coordinate system defines the coordinates used in the radar images presented in this paper.

C. Imaging Algorithm

The radar images are constructed using a backprojection algorithm [28], which is a DAS-type beamformer. The VNA collects the data in the frequency domain. To get a range profile the collected data are transformed to time/range domain using the inverse Fourier transform. The range profile collected with antenna element combination n is denoted $s_n(r)$, and it is a projection of the 3D scene reflectivity along iso-range ellipsoids centered at the phase center of the element combination. The range profile is back projected to each pixel in the image domain to form a sub image, I_n

$$I_n(x_p, y_p) = s_n \left(r | r^2 = x_p^2 + y_p^2 \right). \qquad (8)$$

As illustrated in Fig. 7 $r = r_{tx_n} + r_{rx_n}$, where

$$r_{rx_n} = \sqrt{(x_p - x_{rx_n})^2 + y_p^2} \qquad (9)$$

and

$$r_{tx_n} = \sqrt{(x_p - x_{tx_n})^2 + y_p^2}. \qquad (10)$$

x_{tx_n} and x_{rx_n} are the positions of the respective Tx and Rx element in combination n.

The image, I, is obtained by summation of the sub images from each antenna combination

$$I(x_p, y_p) = \sum_{n=1}^{N_a} I_n(x_p, y_p) \qquad (11)$$

where N_a is the number of antenna combinations used. It is assumed that all reflectors in the scene are stationary within the

TABLE IV
SWITCH PATTERN 56[1]

		Tx							
		1	2	3	4	5	6	7	8
Rx	1		2	4	6	8	12	18	32
	2	1		10	14	17	22	31	42
	3	3	9		20	24	30	36	46
	4	5	13	19		29	34	41	50
	5	7	16	23	28		38	44	52
	6	11	21	27	33	37		48	54
	7	15	26	35	40	43	47		56
	8	25	39	45	49	51	53	55	

time it takes to collect the range profiles, $s_1(r)$ to $s_{N_a}(r)$, and I is assumed to be a snap-shot at time t_i. Continuous radar recordings are used to make a time-lapse data cube, D, of images

$$D(x_p, y_p, t_i) = I_i(x_p, y_p, t_i), \quad i = 1, 2, \ldots, N_f \qquad (12)$$

where N_f is the number of images in the data cube.

D. Antenna Configuration—Switch Pattern

The switch pattern were all 56 combinations are used is given in Table IV. The combinations are sorted by increasing position of the corresponding virtual element defined in (1). We use this pattern as it is the one that fully utilize the antenna array and theoretically will give the highest antenna gain.

In addition to switch pattern 56 we want to find a pattern with fewer elements so that the frame rate, $\mathrm{FR} = (\mathrm{PRF}/N_a)$, is increased. The slow frame rate of switch pattern 56 can lead to badly focused images because the snap-shot assumption described in Section III.C becomes invalid. Even though good quality images are obtained the sampling rate can be too low to capture the details of the heart motion.

To reduce the number of element combinations we use the virtual array defined in Section II.C. The virtual array has 23 unique elements, and by removing the redundant elements we have reduced the length of the switch pattern from 56 to 23 without reducing the spatial sampling properties of the antenna array. We have used the following procedure to do this reduction:

1) For all combinations with equal virtual element position, select those who have the smallest distance between the transmitting and receiving element.
2) Select the combination where the receiving element is closest to the antenna center.

By applying this procedure we get the switch pattern illustrated in Table V, which as for switch pattern 56 is sorted with increasing virtual element positions. The frame rates achieved with these patterns are listed in Table II.

[1]The normal faced numbers describes the order in which a given antenna combination is used, e.g. in the square referenced by Rx—element 1 and Tx element 2 the number 1 indicates that this antenna combination is the first one used in the switch pattern.
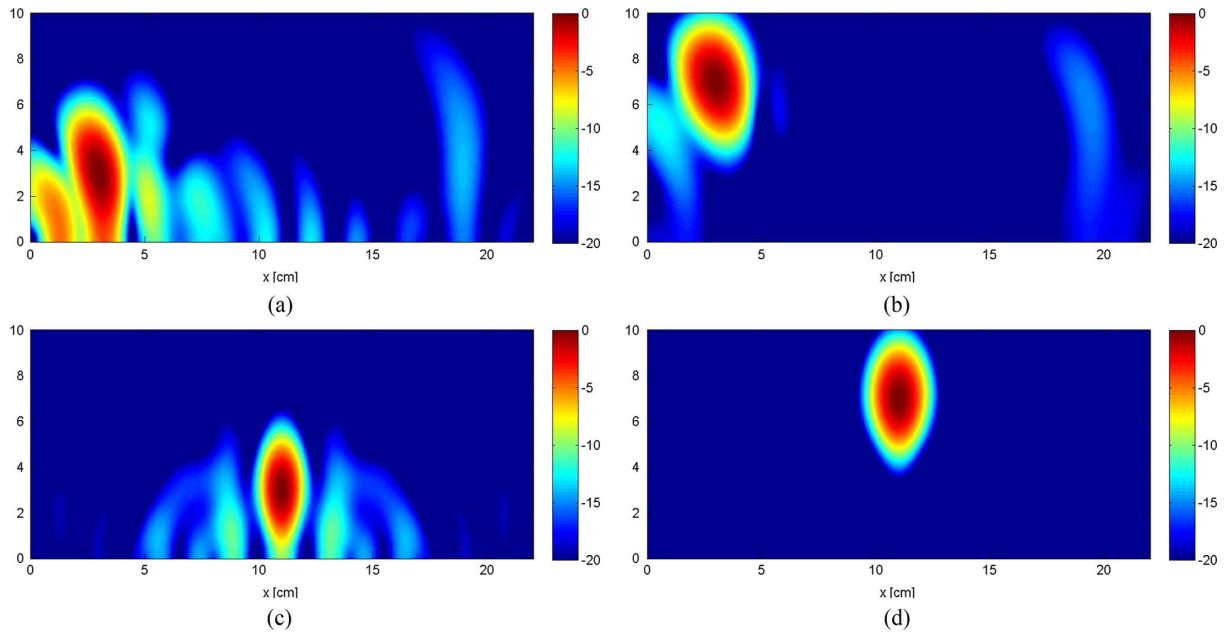
Fig. 8. PSFs for single targets at different locations. Switch pattern 56 are used when generating the images. (a) $x = 3$ cm, $y = 3$ cm. (b) $x = 3$ cm, $y = 7$ cm. (c) $x = 11$ cm, $y = 3$ cm. (d) $x = 11$ cm, $y = 7$ cm.
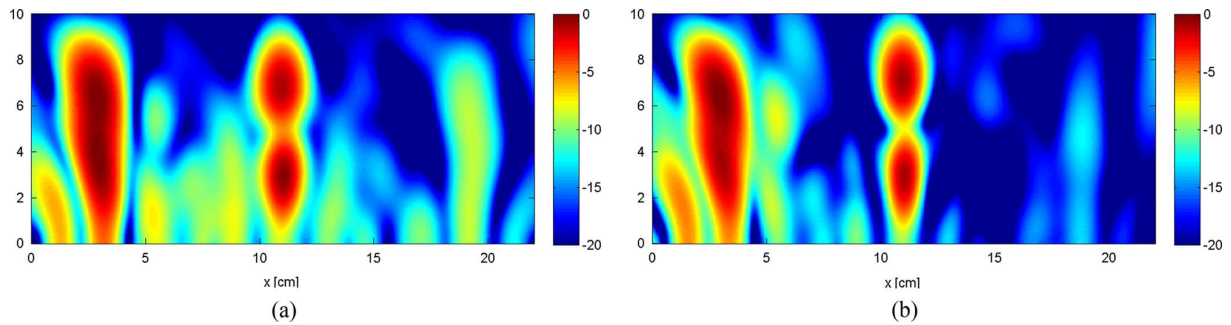

Fig. 9. Point spread function for 4 targets simultaneously at x = 3 and 11 cm and y = 3 and 7 cm. The targets are imaged with both switch pattern 56 and switch pattern 23. (a) Switch pattern 23. (b) Switch pattern 56.

TABLE V
SWITCH PATTERN 23[1]

		Tx							
		1	2	3	4	5	6	7	8
Rx	1	■							
	2	1	■						
	3	2	5	■				14	18
	4	3	7	9	■	12	13	16	20
	5	4	8	11		■	15	17	21
	6	6	10				■	19	22
	7							■	23
	8								■

E. PSF

To analyze the performance of the imaging system, simulated point targets are imaged with both switch patterns. The results are presented in Figs. 8 and 9. In both Figures we see

that the PSFs are dependent on the positions of the target. The resolution in the x-direction is better close to the antenna because the angular coverage increases, see Fig. 8(c) and (d). As the angular coverage increases the angular sampling interval decreases, giving spatial aliasing and increased grating lobe levels. The grating lobes are visible in the lower left corner when the target is in the extreme locations of the imaged area as in Fig. 8(a), (b) and (c).

The resolution in the y-direction is best along the line perpendicular to the antenna going through the antenna center (i.e., the line $x = 11$ cm). In other directions the resolution decreases in the x direction because of the projection of the range vector onto the y-axis. This effect can be seen in Fig. 9(a) and (b), where the targets at $x = 3$ cm are less resolved than the targets at $x = 11$ cm. In Fig. 9(a) and (b) we also see the difference of using switch pattern 56 and 23. The targets are similarly resolved with both switch patterns, but the grating lobes are less visible with switch pattern 56. This can be explained by a higher suppression of the grating lobes because more elements are used, and that virtual array concept used to reduce the switch pattern is more erroneous for targets close to the antenna.

IV. SIGNAL PROCESSING

A. Calibration

To remove the response from cables and switch system the measured data were divided by calibration measurements. The calibration measurements were done by connecting the Tx and Rx channel together at the antenna terminals, and measuring the response, $S_{\text{through}}(f)$. The antenna was removed during this procedure and a short coax cable was used to connect Tx to Rx. The response of this cable, $S_{\text{cable}}(f)$, was measured by connecting it directly to the ports of the VNA. The measured radar data $S_{\text{meas}}(f)$ were then calibrated as

$$S(f) = S_{\text{meas}}(f) \frac{S_{\text{cable}}(f)}{S_{\text{through}}(f)} \qquad (13)$$

where $S(f)$ is the data fed to the imaging algorithm. In addition to remove the response from the switch and the cables, this procedure sets the zero range for the radar measurements at the antenna terminals.

B. Antenna Gain Compensation

The calibration procedure above does not include the antenna. Since the antenna behaves very differently when in contact with the human body compared to the free space response [23], the antenna must be characterized with the human body present. This is practically impossible since we cannot place a reference antenna inside the human body to perform this characterization.

To compensate for different beam patterns between the elements, and different path loss for the individual antenna element combinations, an adaptive algorithm was developed to equalize the signal strength between the antenna combinations. The algorithm starts with the data cube of calibrated data as described in (13). $S_n^i(f)$ is the collected data with antenna combination n in the i'th frame.

1) Remove static reflectors by subtracting the mean

$$X_n^i(f) = S_n^i(f) - \operatorname*{mean}_i \left\{ S_n^i(f) \right\}.$$

2) Calculate the mean over slow time (i.e., index i)

$$\tilde{X}_n(f) = \operatorname*{mean}_i \left\{ X_n^i(f) \right\}.$$

3) Compute the range profiles

$$\tilde{s}_n(r) = F^{-1} \{ \tilde{X}_n(f) \}.$$

4) Find the maximum amplitude for each antenna combination

$$a_n = \max_r (\tilde{s}_n(r)).$$

5) Calculate the gain profile

$$g_n = \frac{\max_n(a)}{a_n},$$

C. Estimation of Heart Motion

Extracting the complex value from the same pixel of every image in the time-lapse data cube of images gives a signal describing the time variation of the signal at the location corresponding to the selected pixel. We denote this signal the slow time profile $p_{xy}(t_i)$

$$p_{xy}(t_i) = D(x_p = x, y_p = y, t_i). \qquad (14)$$

Small movements of an ideal point reflector would cause a phase modulation in the slow time profile proportional to the radial motion of the reflector seen from the antenna phase center. In reality it is more complicated. The image is a projection of a 3D scene onto the 2D image plane, and the modulation in the slow time profile will not stem from the motion of a single point reflector. An algorithm for estimating the heart induced motion of the chest surface from continuous wave radar measurement was presented in [29]. Further analysis is required to develop a similar model for the modulation in the case of body-contact UWB radar. However, it is reasonable to assume that modulations observed in the phase of the slow time profile will be strongly influenced by the heart motion, and we use this as an indicator for the heart motion defined as

$$h_{xy}(t_i) \approx \tan^{-1} \left(\frac{\operatorname{Im}\{p_{xy}(t_i)\}}{Re\{p_{xy}(t_i)\}} \right). \qquad (15)$$

V. RESULTS

A. Switch Pattern 56

In Fig. 10 one of the images from the time-lapse data cube is shown. A movie was made of the time-lapsed images where a rhythmic motion is visible. The observed motion is most clear around the reflectors at locations x = 5 − 15 cm and y = 4 − 10 cm. These are the positions where the heart is expected to be, and the shape of the reflections corresponds well with the shape of the heart wall. The strong reflectors at x = 3 − 19 cm and y = 0 − 4 cm are more or less stationary. Some motions are observed along the edges of the images, particularly at deeper positions.

Slow time profiles were extracted at the four different positions marked in Fig. 10, and the heartbeat motion were estimated according to (15). The results are shown in Fig. 11 were the estimates are plotted together with synchronized ECG recordings. Three heartbeat cycles are shown.

B. Switch Pattern 23

In Fig. 12 an image from the time-lapse imaging using switch pattern 23 is shown. A movie was constructed from the dataset. The signals from the deeper positions are weaker compared to the results when using switch pattern 56, but the same rhythmic motion is observed in the reflectors deeper than y = 4 cm. The motion with switch pattern 56 is more pronounced and concentrated in the x direction.

The heartbeat motions from the four positions marked in Fig. 12 are shown in Fig. 13 together with ECG recordings.

C. Antenna Gain Compensation

To see the effect of the antenna gain compensation described in Section IV.B, the same data used to generate the image in Fig. 10 was used to process an image where the antenna gain
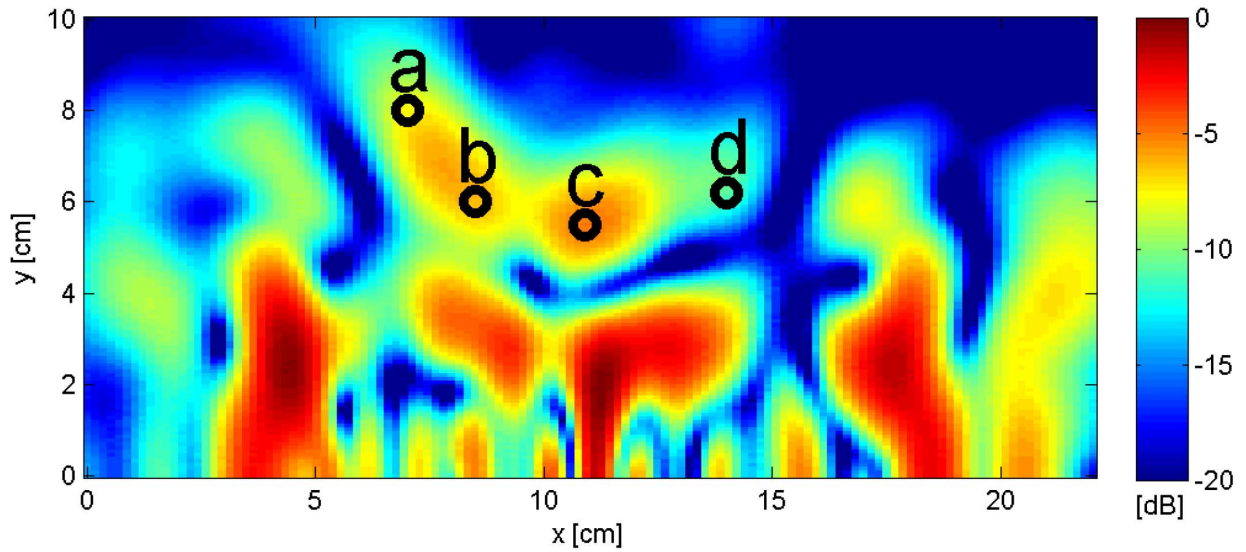
Fig. 10. A single image when using switch pattern 56.

(a) Phase at x = 7.0 cm and y = 8.0 cm.

(b) Phase at x = 8.5 cm and y = 6.0 cm.

(c) Phase at x = 10.9 cm and y = 5.5 cm.
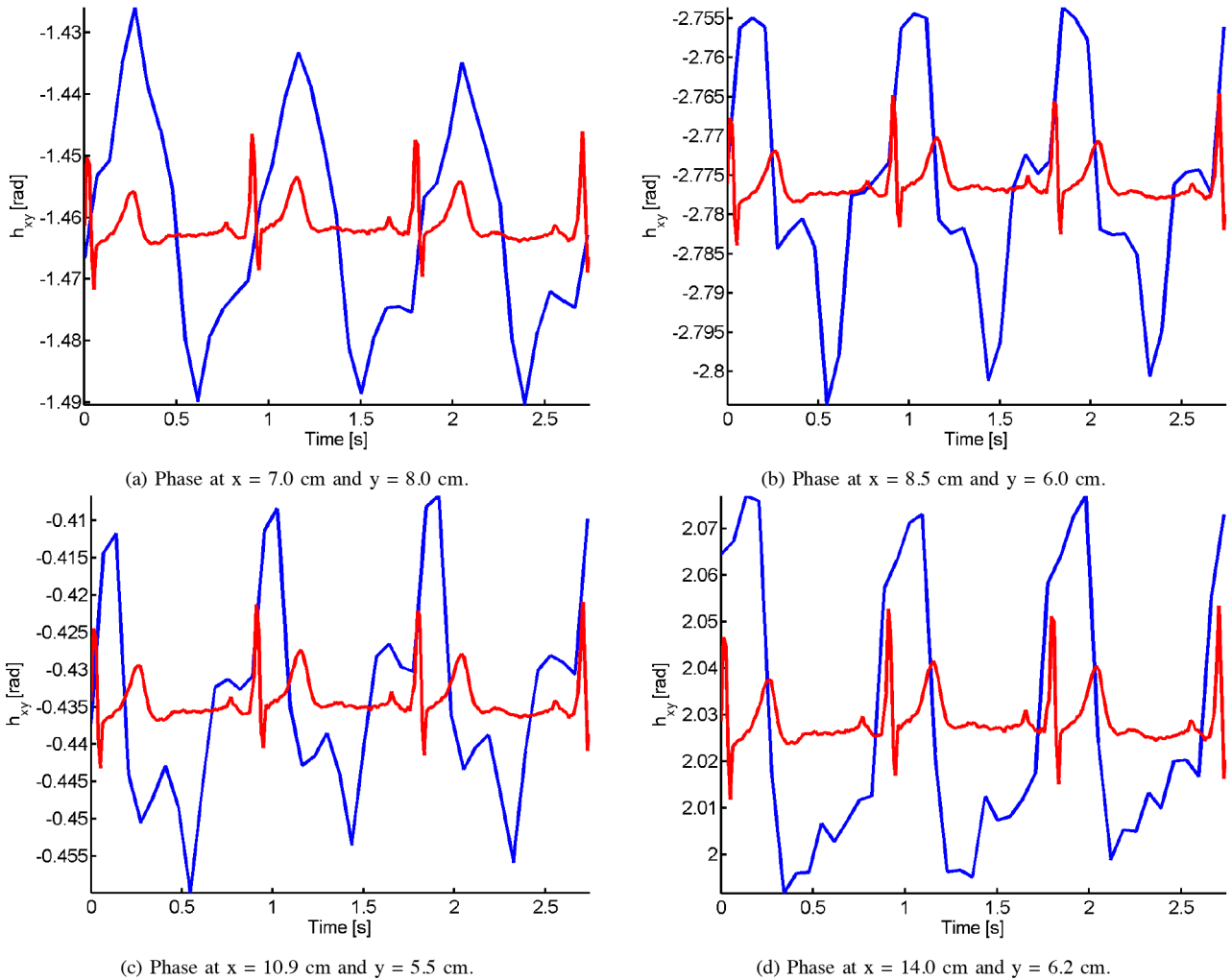
(d) Phase at x = 14.0 cm and y = 6.2 cm.

Fig. 11. Phase modulation estimation from the marked points in Fig. 10. The ECG data is plotted in red and scaled in amplitude to make the plots readable. The given y-axis applies to the radar data only.

compensation was not applied. The resulting image is shown in Fig. 14. In this image the deep reflectors observed in Fig. 10 have almost vanished, and the image is dominated by the strong returns near the antenna center.
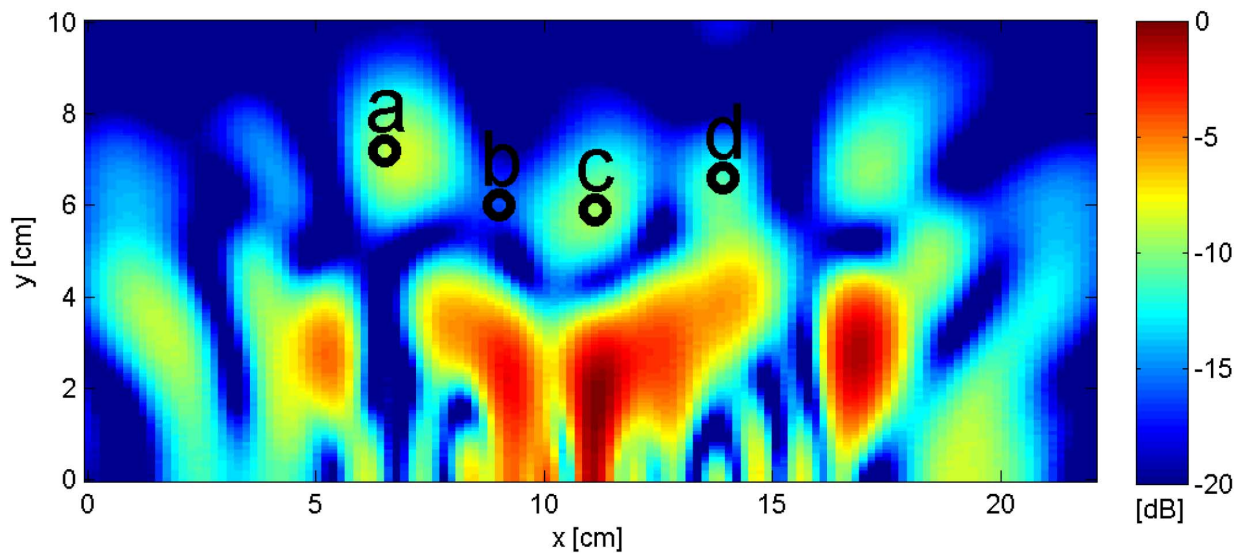
Fig. 12. A single image when using switch pattern 23.

(a) Phase at x = 6.5 cm and y = 7.2 cm

(b) Phase at x = 9.0 cm and y = 6.0 cm

(c) Phase at x = 11.1 cm and y = 5.9 cm
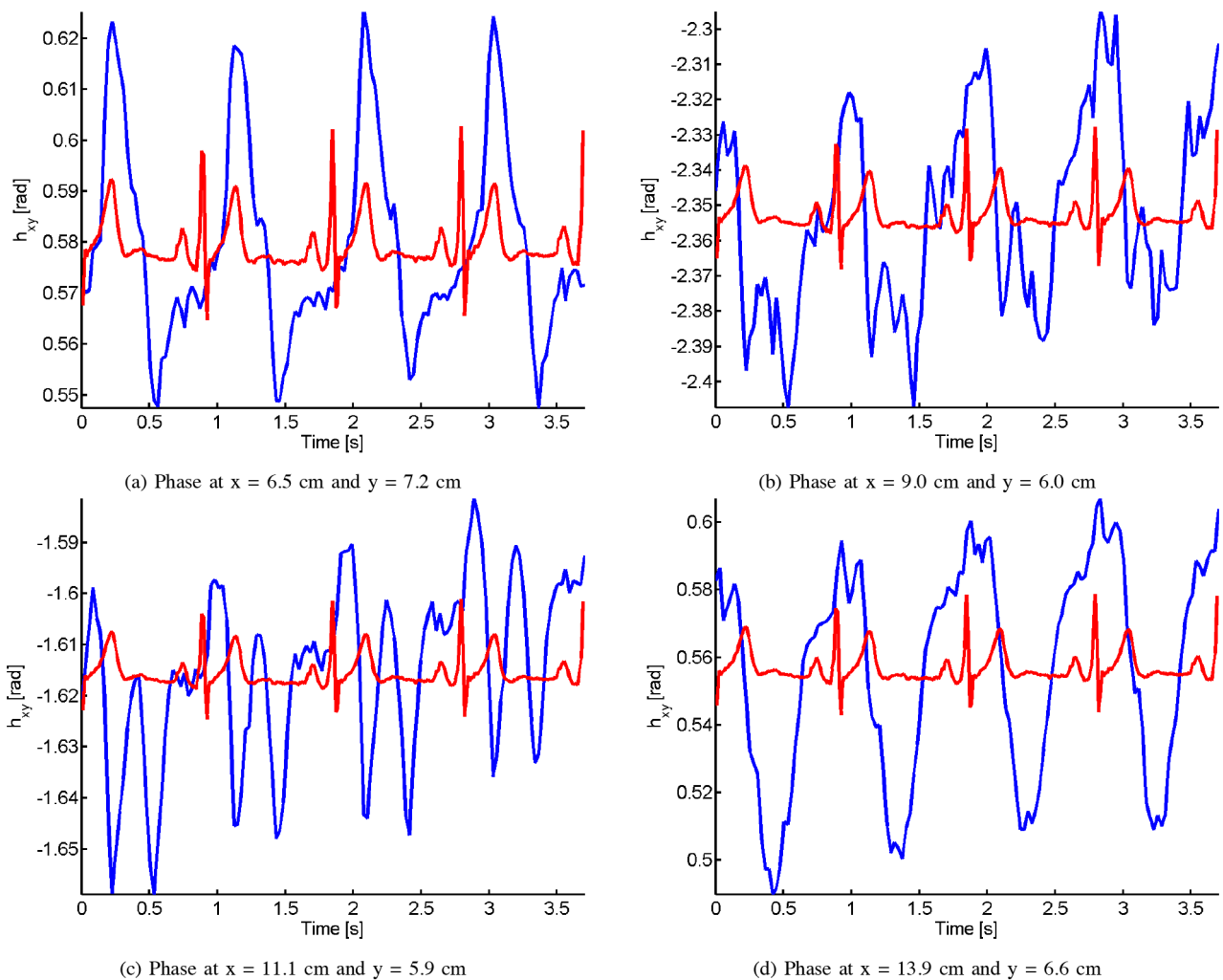
(d) Phase at x = 13.9 cm and y = 6.6 cm

Fig. 13. Phase modulation estimation from the marked points in Fig. 12. The ECG data is plotted in red and scaled in amplitude to make the plots readable. The given y-axis applies to the radar data only.
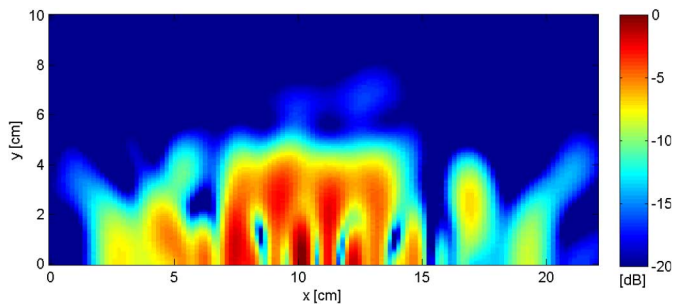
Fig. 14.   Image with no antenna gain compensation, using the same data that were used to form the image in Fig. 10.

VI. DISCUSSION

A. Antenna Gain Compensation

In [19] and [7] the radar data was high-pass filtered to remove static reflectors so that the dynamic heartbeat signal could be detected. The heart's motion is cyclic and in the points in time where the velocity of the heart is zero, the high-pass filter will remove the signal from the heart as well. This is particularly visible when creating a time-lapse movie as it was done in [19]. The filter will attenuate slow moving reflectors, and the fast moving ones will be more pronounced, causing a more chaotic heart motion in the movie. Using the antenna gain compensation proposed in this paper we are able to detect the heart motion without using a high-pass filter. This results in a better representation of the heart motion in the movies.

As seen in Fig. 14 the heart is almost invisible when the imaging is done without gain compensation. The radar geometry is different for the different antenna combinations. For element combinations with short separation their individual beam patterns will overlap more, giving higher antenna gain than for combination with longer element separation. There will also be differences in the length of travel between a reflector and the elements in the different element combinations. Due to high attenuation of human tissues this can lead to differences in the signal levels for the different element combinations. Without gain compensation element combinations with weak signals does not contribute to the image formation and the image is dominated by the strong reflectors near the antenna center as seen in Fig. 14.

B. Imaging of the Heart

It is hard to present concluding evidence of what is actually seen in the images presented in this paper. We have no exact knowledge of the distribution of the different body tissues and location of potential reflectors that can be identified in the images. However, the reflectors around the marked points in Figs. 10 and 12 correspond well with the expected location and size of the heart wall. These are also the areas with most pronounced motion indicating that it is the heart that is seen.

Comparing the phase modulations in Figs. 11 and 13 with the ECG measurement it is clear that the modulation seen corresponds to the heart cycle. The shape of the modulation is repeating from cycle to cycle suggesting that the signals contain more information than just the heartbeat rate. More details are

seen in Fig. 13 because higher frequency components are captured due to higher sampling rate. Increasing the *PRF* of the radar system can therefore be important in further development of the radar system. We also experience variation in the signals depending on the spatial location in the images. The shape and the timing of the highest peak in the radar signal compared to the highest peak in the ECG signal differs, indicating that different parts of the heart are modulating the radar signal. The shape of the phase modulation waveforms may provide valuable information to medical doctors [7]. Further studies should be carried out to investigate the content of information in these signals.

The image with switch pattern 56, Fig. 10, gives better results in terms of visual image quality, especially at the deeper positions. This can be expected since more than twice the antenna element combinations are used compared to the image in Fig. 12. The cost is the reduced frame rate and sampling rate of the phase estimate waveforms.

VII. CONCLUSION

A proof of concept for UWB time-lapsed radar imaging of the human heart is demonstrated. The results are promising and there is good indication that the moving heart wall is seen in the images. Further studies are required to confirm this and to assess the medical value of the information. By comparing the modulation at specific locations in the images with ECG data it is confirmed that the modulation seen is related to the heart motion. The modulation shows signs of containing detailed information about the cardiac cycle and is dependent on the spatial location. If important events of the cardiac cycle can be connected to these signals, microwave imaging of the heart may well provide an additional observation mode for improved heart diagnostics. The radar system presented, with the parameters and their trade-offs, is a good basis for further development of UWB medical radar system and circuits for heart imaging.

REFERENCES

[1] WHO "Global atlas on cardiovascular disease prevention and control," World Health Organization, 2011. [Online]. Available: http://www.who.int/cardiovascular_diseases/publications/atlas_cvd/en/index.html

[2] Ø Aardal, Y. Paichard, S. Brovoll, T. Berger, T. S. Lande, and S.-E. Hamran, "Physical working principles of medical radar," *IEEE Trans. Biomed. Eng.*, vol. 60, no. 4, pp. 1142–1149, 2013.

[3] C. Li, V. Lubecke, O. Boric-Lubecke, and J. Lin, "A review on recent advances in doppler radar sensors for noncontact healthcare monitoring," *IEEE Trans. Microw. Theory Tech.*, vol. 61, no. 5, pp. 2046–2060, May 2013.

[4] D. Zito, D. Pepe, M. Mincica, F. Zito, A. Tognetti, A. Lanata, and D. De-Rossi, "SoC CMOS UWB pulse radar sensor for contactless respiratory rate monitoring," *IEEE Trans. Biomed. Circuits Syst.*, vol. 5, no. 6, pp. 503–510, Dec. 2011.

[5] Ø. Aardal, S.-E. Hamran, T. Berger, J. Hammerstad, and T. S. Lande, "Radar cross section of the human heartbeat and respiration in the 500 mhz to 3 GHz band," in *Proc. IEEE Radio and Wireless Symp.*, 2011, pp. 422–425.

[6] J. A. J. Thijs, J. Muehlsteff, I. Such, R. Pinter, R. Elfring, and C. H. Igney, "A comparison of continuous wave Doppler radar to impedance cardiography for analysis of mechanical heart activity," in *Proc. IEEE Conf. Engineering in Medicine and Biology Soc.*, 2005, pp. 3482–3485.

[7] Ø. Aardal, S. Brovoll, Y. Paichard, T. Berger, T. S. Lande, and S.-E. Hamran, "Detecting changes in the human heartbeat with on-body radar," in *Proc. IEEE Radar Conf.*, Apr. 2013, pp. 1–6.

[8] J. Muehlsteff, J. Thijs, R. Pinter, G. Morren, and G. Muesch, "A hand-held device for simultaneous detection of electrical and mechanical cardio-vascular activities with synchronized ECG and CW-Doppler radar," in *Proc. IEEE Conf. Engineering in Medicine and Biology Soc.*, Aug. 2007, pp. 5758–5761.

[9] P. Meaney, M. Fanning, D. Li, S. Poplack, and K. Paulsen, "A clinical prototype for active microwave imaging of the breast," *IEEE Trans. Microw. Theory Tech.*, vol. 48, no. 11, pp. 1841–1853, Nov. 2000.

[10] T. Grzegorczyk, P. Meaney, P. Kaufman, R. di Florio-Alexander, and K. Paulsen, "Fast 3-d tomographic microwave imaging for breast cancer detection," *IEEE Trans. Med. Imag.*, vol. 31, no. 8, pp. 1584–1592, Aug. 2012.

[11] E. Fear, J. Bourqui, C. Curtis, D. Mew, B. Docktor, and C. Romano, "Microwave breast imaging with a monostatic radar-based system: A study of application to patients," *IEEE Trans. Microw. Theory Tech.*, vol. 61, no. 5, pp. 2119–2128, May 2013.

[12] M. Klemm, I. Craddock, J. Leendertz, A. Preece, and R. Benjamin, "Radar-based breast cancer detection using a hemispherical antenna array 2014;experimental results," *IEEE Trans. Antennas Propag.*, vol. 57, no. 6, pp. 1692–1704, Jun. 2009.

[13] T. Henriksson, M. Klemm, D. Gibbins, J. Leendertz, T. Horseman, A. Preece, R. Benjamin, and I. Craddock, "Clinical trials of a multi-static uwb radar for breast imaging," in *Proc. Antennas and Propagation Conf.*, Loughborough, U.K., Nov. 2011, pp. 1–4.

[14] W. C. Khor and M. Bialkowski, "Investigations into an uwb microwave radar system for breast cancer detection," in *Proc. IEEE Antennas and Propagation Soc. Int. Symp.*, Jun. 2007, pp. 2160–2163.

[15] Y. Chen, E. Gunawan, K. S. Low, S. C. Wang, Y. Kim, and C.-B. Soh, "Pulse design for time reversal method as applied to ultrawideband microwave breast cancer detection: A two-dimensional analysis," *IEEE Trans. Antennas Propag.*, vol. 55, no. 1, pp. 194–204, Jan. 2007.

[16] S. Semenov, R. Svenson, A. Boulyshev, A. Souvorov, V. Borisov, Y. Sizov, A. Starostin, K. Dezern, G. Tatsis, and V. Baranov, "Microwave tomography: Two-dimensional system for biological imaging," *IEEE Trans. Biomed. Eng.*, vol. 43, no. 9, pp. 869–877, 1996.

[17] H. Hjortland and T. Lande, "Ctbv integrated impulse radio design for biomedical applications," *IEEE Trans. Biomed. Circuits Syst.*, vol. 3, no. 2, pp. 79–88, Apr. 2009.

[18] B. Neri and S. Saponara, "Advances in technologies, architectures, and applications of highly-integrated low-power radars," *IEEE Aerosp. Electron. Syst. Mag.*, vol. 27, no. 1, pp. 25–36, Jan. 2012.

[19] S. Brovoll, T. Berger, Y. Paichard, Ø. Aardal, T. Lande, and S.-E. Hamran, "Time-lapse imaging of human heartbeats using uwb radar," in *Proc. IEEE Biomedical Circuits and Systems Conf.*, Oct. 2013, pp. 142–145.

[20] M. J. Øyan, S.-E. Hamran, T. Berger, and L. Hanssen, "Characterisation of ultra wideband frequency modulated and step frequency radar with range gating," in *Proc. IASTED Conf.*, Jul. 2009, ARP2009.

[21] C. A. Balanis, *Advanced Engineering Electromagnetics*. Hoboken, NJ, USA: Wiley, 1989.

[22] S. M. Salvador and G. Vecchi, "Experimental tests of microwave breast cancer detection on phantoms," *IEEE Trans. Antennas Propag.*, vol. 57, no. 6, pp. 1705–1712, 2009.

[23] S. Brovoll, Ø. Aardal, Y. Paichard, T. Berger, T. Lande, and S.-E. Hamran, "Optimal frequency range for medical radar measurements of human heartbeats using body-contact radar," in *Proc. 35th Annu. Int. Conf. IEEE Engineering in Medicine and Biology Soc.*, Jul. 2013, pp. 1752–1755.

[24] E. M. Staderini, "UWB radars in medicine," *IEEE Aerosp. Electron. Syst. Mag.*, vol. 17, no. 1, pp. 13–18, Jan. 2002.

[25] C. Gabriel and L. D. O. P. King's College, *Compilation of the Dielectric Properties of Body Tissues at RF and Microwave Frequencies*. London, U.K.: King's College, 1996, Dept. Physics.

[26] D. Andreuccetti, R. Fossi, and C. Petrucci, An Internet Resource for the Calculation of the Dielectric Properties of Body Tissues in the Frequency Range 10 hz–100 ghz, 1997 [Online]. Available: http://niremf.ifac.cnr.it/tissprop/

[27] F. J. Baisch and R. Gerzer, "Positive pressure breathing by total body negative pressure: A new simulation model for fluid balance in weightlessness?," *Acta Astron.*, vol. 54, no. 9, pp. 649–655, 2004.

[28] T. Berger, S. Hamran, Y. Paichard, and Ø. Aardal, "Close range ultra wideband microwave imaging in a non-homogeneous background," in *Proc. IASTED Int. Conf. Signal and Image Processing*, 2011.

[29] Ø. Aardal, S.-E. Hamran, T. Berger, Y. Paichard, and T. S. Lande, "Chest movement estimation from radar modulation caused by heartbeats," in *Proc. IEEE Biomedical Circuits and Systems Conf.*, 2011, pp. 422–425.

Sverre Brovoll received the M.Sc. degree in cybernetics from the Norwegian University of Science and Technology, Trondheim, Norway, in 2006.

In 2006, he started working with synthetic aperture radar systems as a Scientist at the Norwegian Defence Research Establishment (FFI), Kjeller, Norway. In 2011, he began working toward the Ph.D. degree in the field of medical radar systems at FFI and in the Department of Informatics, University of Oslo, Oslo, Norway.

Tor Berger received the M.Sc. and Ph.D. degrees in applications of the wavelet transform in image processing from the University of Tromsø, Tromsø, Norway, in 1992 and 1996, respectively.

Since 1996, he has been with the Norwegian Defence Research Establishment, Kjeller, Norway, working in different fields such as weapon effects, security sensors, and signal processing. He is currently involved in radar signal processing related to ultra wideband systems and synthetic aperture radar.

Yoann Paichard (M'05) received the M.Eng. degree in electrical engineering from the National Institute of Applied Science, Rennes, France, the M.Sc. degree in electronics and communications systems from the University of Pierre and Marie Curie, Paris, France, and the Ph.D. degree in physics from the University of Paris-Sud, Orsay, France, in 2001, 2003, and 2007, respectively.

From 2003 to 2007, he carried out research at the French Aerospace Lab, Onera, France, on ultra-wideband radars and on real-time imaging radars applied to micro-Doppler measurements. In 2008, he joined the Radar Remote Sensing Group as a Lecturer at the University of Cape Town, Cape Town, South Africa, where he was involved in the design of passive coherent location radars and multistatic radars. Since 2010, he has been with the Norwegian Defence Research Establishment, Kjeller, Norway, where he is doing research on remote sensing of vital signs using radar techniques. His research interests include the design of radars, antennas, and microwave systems.

Øyvind Aardal received the M.Sc. degree in applied mathematics from the University of Oslo, Oslo, Norway, and the Ph.D. degree from the Norwegian Defence Research Establishment (FFI), Kjeller, Norway, in 2008 and 2013, respectively.

In summer 2007, he was a Lecturer in mathematics at Oslo University College, Oslo, Norway. Since 2009, he has been with FFI, where he is currently working as a Scientist. His research interests include radar signal processing, target recognition and medical radar.

Tor Sverre Lande (F'10) is a Professor of microelectronics in the Department of Informatics, University of Oslo, Oslo, Norway, as well as a Visiting Professor at the Institute of Biomedical Engineering, Imperial College, London, U.K.

His primary research is related to microelectronics, both digital and analog. Research fields are neuromorphic engineering, analog signal processing, subthreshold circuit and system design, biomedical circuits and systems, and impulse radio (UWB). He is the author or coauthor of more than 150 scientific publications with chapters in two books.

Mr. Lande is serving as an Associate Editor of several scientific journals and as Guest Editor of special issues, including IEEE TRANSACTIONS ON CIRCUITS AND SYSTEMS, VOL. II and IEEE TRANSACTIONS ON CIRCUITS AND SYSTEMS, VOL. I, special issue on "Biomedical Circuits and Systems." He is/has been a technical committee member of several international conferences and has served as reviewer for a number of international technical journals. He has served as the Technical Program Chair for the IEEE International Symposium on Circuits and Systems (ISCAS), Bangkok, Thailand, in 2003, NORCHIP, Oslo, Norway, in 2004, the IEEE International Workshop on Biomedical Circuits and Systems (BioCAS), Singapore, in 2004, BioCAS, U.K., in 2006, and ISCAS 2011. He was the Chair-Elect of the BioCAS technical committee from 2003–2005. He is also a member of other IEEE Circuits and Systems Society (CAS) technical committee. In 2006, he became a Distinguished Lecturer of the CAS and was an elected member of the CAS Board of Governors. He is currently serving as the Vice President of Conferences in the CAS Society. He was also the founding Editor-in-Chief of the IEEE TRANSACTIONS ON BIOMEDICAL CIRCUITS AND SYSTEMS from 2007–2010.

Svein-Erik Hamran received the M.Sc. degree in technical physics from the Norwegian Institute of Technology, Trondheim, Norway, and the Dr.Sci. degree in applied physics from the University of Tromsø, Tromsø, Norway, in 1984 and 1990, respectively.

From 1985 to 1996, he was with the Environmental Surveillance Technology Programme and was a Visiting Scientist at CNRS Service d'Aeronomie, Paris, France, during 1989–1990. Since 1996, he has been at the Norwegian Defence Research Establishment, Kjeller, Norway, working as a Chief Scientist managing radar programs. From 2001 to 2011, he was an Adjunct Professor in Environmental Geophysics in the Department of Geosciences, University of Oslo, Oslo, Norway. Since 2011, he has been an Adjunct Professor in the Department of Informatics at the University of Oslo. He is the Principal Investigator on the Radar Imager for Mars subsur FAce eXperiment RIMFAX on the Mars 2020 NASA rover mission and a Co-Principal Investigator on the WISDOM ground penetrating radar (GPR) experiment on the ESA ExoMars rover. His main interests are UWB radar design, radar imaging, and modelling in medical and GPR.